Journal of Computational Electronics (2026) 25:132
https://doi.org/10.1007/s10825-026-02582-9

RESEARCH

Shape-aware dissimilarity measures for process TCAD model calibration

Roman Kostal[1] · Tobias Reiter[1,2] · Stefano Di Nicola[3] · Manuel Kleinbichler[4] · Paul Manstetten[1] · Lado Filipovic[1,2]

Received: 26 February 2026 / Accepted: 3 June 2026

Abstract

Traditional calibration of semiconductor TCAD models for topography modifying processes often relies on matching critical dimensions (CDs). This approach is prone to subjective measurement and fails to capture overall profile shape differences, thereby limiting the accuracy and effectiveness of model optimization. In this work, we address this limitation by adapting computer vision techniques for TCAD model calibration. We comprehensively evaluate several shape dissimilarity measures (SDM): the established Chamfer Distance (CHD) and two novel level-set-based measures, the Area Difference (AD) and the Sparse Field Distance (SFD). Through a rigorous computational case study, testing for sensitivity, robustness, and efficiency, we demonstrate that SFD and CHD significantly outperform traditional CD matching and area-based methods for semiconductor profile comparison derived from a representative scanning electron microscopy (SEM) image. These standardized SDMs are crucial for leveraging emerging large-scale electron microscopy datasets and enabling robust, machine learning-driven model development.

Keywords Process TCAD simulation · Process optimization · Level-set methods · Shape dissimilarity measures · Semiconductor fabrication · Computer vision · Computational geometry

1 Introduction

Process TCAD calibration for topography-modifying processes, such as deposition and etching, is typically formulated as an optimization problem where the decision variables are model parameters and the loss function measures the discrepancy between simulated and target feature profiles. A common construction relies on a set of critical dimensions (CDs), which are scalar geometric descriptors such as depth, width at specific heights, and sidewall angles, measured at predetermined locations [1, 2]. For the structure in Fig. 1a, the objective function L used to optimize the decision variables of the simulation model is then the weighted root mean square deviation (RMSD) of the corresponding CDs:

$$L = \sqrt{\begin{aligned} &\sum_{i\in\{m,t,f\}} a_{wi}(\hat{w}_i - w_i)^2 \\ &+ \sum_{j\in\{m,f\}} a_{hj}(\hat{h}_j - h_j)^2 \\ &+ a_{ah}(\hat{a}_h - a_h)^2 \end{aligned}}, \tag{1}$$

where w_m is the width of the mask opening, w_t is the width at the top of the feature, w_f measures bowing or tapering, h_m is

✉ Roman Kostal
kostal@iue.tuwien.ac.at

Tobias Reiter
reiter@iue.tuwien.ac.at

Stefano Di Nicola
stefano.dinicola@infineon.com

Manuel Kleinbichler
manuel.kleinbichler@k-ai.at

Paul Manstetten
manstetten@iue.tuwien.ac.at

Lado Filipovic
filipovic@iue.tuwien.ac.at

[1] Institute for Microelectronics, TU Wien, Gußhausstraße 25-27, Vienna 1040, Austria

[2] CDL for Multi-Scale Process Modeling of Semiconductor Devices and Sensors, TU Wien, Gußhausstraße 25-27, Vienna 1040, Austria

[3] Infineon Technologies Austria AG, Siemensstraße 2, Villach 9500, Austria

[4] KAI – Kompetenzzentrum Automobil- und Industrieelektronik GmbH, Europastraße 8, Villach 9524, Austria

Published online: 18 June 2026

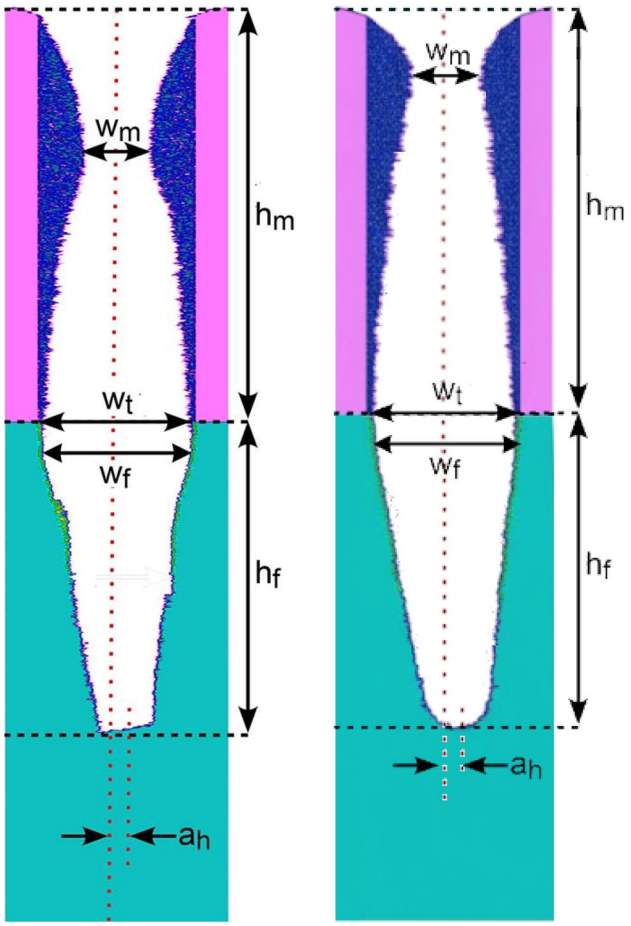

(a) Comparison of two profiles with identical scalar CDs.[1]

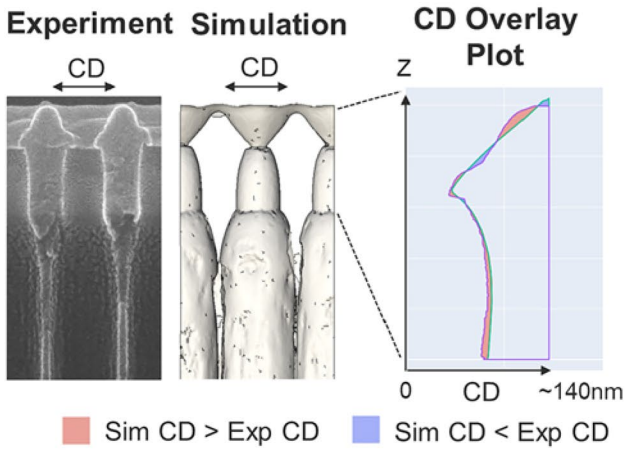

(b) Intersection over Union (IoU) approach.[2]

Fig. 1 **a** Demonstration of local sampling limitations where distinct profiles yield identical CD values based on the methodology in [1]; **b** alternative global profile comparison using IoU as proposed in [5]. ((1) Reprinted with permission from F. Kr¨uger et al., J. Vac.Sci. Technol. A **42**, 043008 (2024). Copyright 2024, AmericanVacuum Society. (2) Reprinted with permission from T. Nishizuka et al., J. Vac.Sci. Technol. A **42**, 043003 (2024). Copyright 2024, AmericanVacuum Society)

the mask thickness, and h_f is the feature depth. The scalar a_h measures asymmetry, while $a_{w\cdot}$, $a_{h\cdot}$ and a_{ah} are non-negative weight factors. Quantities extracted from scanning electron microscope (SEM) images are denoted by hats.

While CD-based comparison is computationally efficient and conceptually straightforward, it suffers from a key shortcoming: it samples the structure only at isolated locations, resulting in a sparse description of the geometry. This *local sampling* limitation allows substantial profile discrepancies in unmeasured regions to go undetected. Two features may exhibit nearly identical CDs while varying in surface curvature or corner rounding, influencing subsequent process steps and electrical behavior [3] [4]. Figure 1a illustrates a case where a profile differs markedly from the target yet achieves a loss of zero ($L = 0$) because the CDs are identical. Specific examples of features missed by this approach include:

- The metric w_m measures the minimum mask opening but does not anchor its vertical coordinate. Consequently, the “pinch point" can shift significantly along the mask height h_m without being penalized by the optimizer.
- Since widths are only sampled at the top (w_t) and the maximum bowing point (w_f), any deviations between these heights–such as the scalloping typical of Deep Reactive Ion Etching (DRIE) processes–remain undetected.
- The depth metric h_f identifies the etch front, but it cannot distinguish between a rounded “U-shaped" bottom and a flat or “micro-trenched" bottom.
- Metrics h_m and w_m do not capture the specific taper or “rounding" of the mask material, which significantly impacts ion reflection and shadowing deep within the feature.

As fabrication technology advances toward fully three-dimensional (3D) architectures (e.g., FinFETs, gate-all-around FETs, and high-aspect-ratio interconnects), the limitations of CD-based descriptors become more pronounced. The geometry of such structures cannot be adequately represented by scalar measurements. Curved and multi-scale features exhibit complex topologies that are lost in low-dimensional representations. In 3D, the number of CDs required for meaningful comparison grows rapidly, making manual definition impractical.

Recently, Nishizuka et al. [5] proposed an approach based on the intersection over union (IoU) dissimilarity measure for high-aspect-ratio contact (HARC) etch optimization. Their method employs the objective function:

$$L(E, S) = 1 - \text{IoU} = 1 - \frac{|E \cap S|}{|E \cup S|}, \tag{2}$$

where E and S represent the experimental and simulated material profile sets, respectively. By overlaying cross-sections with simulator outputs, they enabled comprehensive profile assessment rather than point-wise sampling (see Fig. 1b).

Nevertheless, several limitations still remain. First, the IoU treats all spatial deviations equally, regardless of their distance from the surface, which can lead to optimization convergence issues when surfaces differ significantly in shape while having near-equal area mismatches. Errors near active regions or interfaces can dominate device behavior [6], making equal treatment of all deviations suboptimal. Second, the lack of described implementation details for profile extraction and spatial alignment limits reproducibility and broader adoption.

To address these gaps, a new approach must deliver global profile assessment and handle arbitrary geometric complexity within an open-source framework. We introduce and evaluate several advanced shape dissimilarity measures (SDMs). This work demonstrates that Sparse Field Distance (SFDT) and Chamfer Distance (CHD) [7] offer superior, shape-aware alternatives to CD and area-based matching, providing the necessary robustness for TCAD model calibration. The computational core for these methods is implemented within the open-source sparse level-set library ViennaLS [8], which serves as the geometric engine for the ViennaPS process simulation framework [9].

2 Implementation details

2.1 Level-set representation

Our methods are implemented in the open-source process simulation framework ViennaPS [8–10], which employs level-set techniques for the implicit representation of surfaces and interfaces [11–13]. In this approach, a material interface ∂M is described by a signed distance function (SDF) $\phi(\mathbf{x}, t)$:

$$\phi(\mathbf{x}, t) = \begin{cases} d, & \mathbf{x} \notin \overline{M} \\ 0, & \mathbf{x} \in \partial M \\ -d, & \mathbf{x} \in M \end{cases}, \tag{3}$$

where d denotes the L^1 distance from $\mathbf{x}$ to the nearest point on the surface ∂M of the material volume $\overline{M}$ at time t. This representation naturally handles topological changes and provides sub-grid accuracy, making it well-suited for semiconductor process simulation involving complex geometries.

To improve memory efficiency, the framework employs a sparse field implementation where precise distance values are maintained only on a subset of points G_w within a narrow band of the surface [14]. Points that do not lie in this region are assigned extreme positive (outside) or negative (inside) values relative to the interface. In addition, the underlying data structure employs Hierarchical Run-Length Encoding (HRLE) [15], which increases efficiency by simplifying the storage of repetitive values while keeping data access fast. The implementation details can be found in [16]. The application of the level-set method using a sparse field to example shapes is shown in Fig. 2a and b.

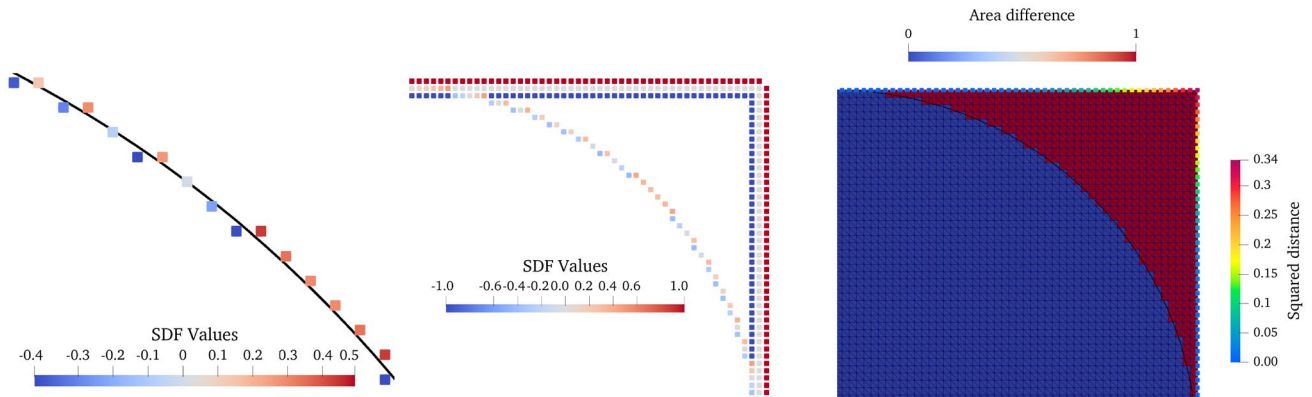

(a) Circular arc: explicit (black) and implicit sparse field.

(b) Implicit quarter circle and square.

(c) Application of the AD and SFDT measures to the shapes in (b).

Fig. 2 Visualization of surface representations by the sparse field and how it can be used to define SDMs for surfaces

The level-set representation inherently supports global shape comparison, as the SDF provides a continuous field for direct geometric evaluation. This capability is the mathematical foundation for the SDMs developed in this work and implemented within the ViennaLS library. As the optimization and calibration tool of the ecosystem, ViennaFit [17] utilizes these implicit domains to perform comprehensive profile comparisons that overcome the limitations of traditional, point-wise CD approaches. Since the SDF is defined over the entire computational domain, these measures are naturally geometry-agnostic, allowing for the calibration of models featuring arbitrary topological complexity, such as the transition from simple trenches to 3D nanosheet architectures, without requiring the manual definition of new scalar descriptors.

2.2 Target profile extraction from experimental images

The target profile $\phi^{\mathcal{T}}$ can be extracted from a SEM or TEM image either by automated image processing or by manual boundary annotation. Automated extraction relies on computer vision techniques such as Canny edge detection [18, 19], which can perform well on high-contrast images with sharp boundary separation. For images with challenging contrast or artifacts, tailored machine learning approaches can improve automated extraction [20]. The manual route is supported directly in ViennaFit through an integrated boundary extractor. The user annotates boundary points that define a directed polygonal chain, from which the level-set representation is generated automatically.

In the present work, the experimental target was obtained by manual boundary annotation. The SEM image was first calibrated to physical units and placed in the same Cartesian coordinate system as the simulation domain. The material interface of interest was then selected as an ordered set of boundary points using the ViennaFit boundary extractor. These points define a directed polygonal chain from which the level-set representation is generated automatically, yielding the signed distance function $\phi^{\mathcal{T}}$.

It is important to note that the accuracy of all SDMs is contingent on the quality of the extracted target profile $\phi^{\mathcal{T}}$. In practice, SEM and TEM images frequently exhibit multiple contrasts arising from layered material stacks, charging artifacts, substrate contributions, or background structures. These contrasts can complicate automated boundary extraction if a strong but irrelevant material interface is mistaken for the process front of interest. Once the profile has been correctly extracted, however, the downstream SDMs operate solely on the geometric representation of the boundary. Thus, image contrast does not enter AD, CHD, SFDT, or CD directly after segmentation; its impact is indirect but important, through the fidelity of the extracted target profile. Careful profile extraction, guided by the user's domain knowledge of the material stack, is therefore a prerequisite for meaningful comparison.

Noise and low resolution in experimental images also primarily affect the boundary extraction step and therefore propagate into any downstream SDM [21, 22]. The full-profile measures evaluated in this work do not eliminate the effects of image uncertainty. Rather, they distribute the effect of boundary perturbations differently than CD-based comparison. CD-based comparison samples only a small number of user-selected locations, so a local artifact or segmentation error at one of these locations can have a disproportionate effect, while deviations away from the selected CDs may be ignored. AD, CHD, and SFDT evaluate the full extracted profile, so isolated local perturbations are averaged over the profile and typically have a smaller relative influence. Systematic errors, such as a consistently misplaced interface caused by poor contrast or insufficient resolution, affect all SDMs and must be controlled at the extraction stage.

Finally, when multiple SEM or TEM images of nominally identical structures are available, ViennaFit [17] supports simultaneous comparison against multiple target profiles. The objective function can be defined as a weighted ensemble average:

$$L = \sum_i w_i \, \ell\left(\phi^{\mathcal{S}}, \phi_i^{\mathcal{T}}\right), \tag{4}$$

where ℓ is the selected SDM, $\phi^{\mathcal{S}}$ is the simulated profile, $\phi_i^{\mathcal{T}}$ are the individual experimentally extracted target profiles, and w_i are user-selected weights. This formulation allows process variability to be included directly in the calibration objective and reduces the sensitivity of the calibration result to any single experimental reference. The same SDMs can also be used to estimate the magnitude of the observed profile variability itself, for example by computing the distribution of pairwise distances between experimentally extracted profiles, provided that the observed spread is dominated by process differences rather than metrology or segmentation artifacts. Such a variability estimate can be used to interpret the calibrated model error: if the optimized simulation lies within the experimental profile-to-profile variability, further reduction of the objective may no longer be physically meaningful.

3 Shape dissimilarity measures

To rigorously evaluate the effectiveness of SDMs for TCAD model calibration, we analyze and implement three practical measures. First, we describe the Area Difference (AD), a global measure conceptually similar to Intersection over Union (IoU) used by Nishizuka et al. [5]. Next, we introduce

a novel Sparse Field Distance (SFD) approach. Both AD and SFD operate directly on the implicit sparse field. Finally, we establish the theoretical basis of the Hausdorff distance (HD) as a benchmark before detailing the Chamfer distance (CHD), which utilizes an explicit surface representation converted from the level-set domain.

3.1 Area difference

The Area Difference (AD) provides a standardized, geometry-agnostic approach for profile comparison that overcomes the fundamental limitations of local sampling. Unlike discrete critical dimension measurements, AD quantifies the total non-overlapping area between target and simulated profiles, offering a global assessment of the entire geometry.

On a 2D grid G^{2D}, each rectangular mesh cell is identified by the position of its lower-left node $\mathbf{x}$. We compute the average SDF value, $\xi(\mathbf{x})$ across the four corners of each cell:

$$\xi(\mathbf{x}) = \frac{1}{4} \sum_{i,j \in \{0,1\}} \phi(\mathbf{x} + i\Delta x \mathbf{e}_1 + j\Delta x \mathbf{e}_2), \tag{5}$$

where $\mathbf{e}_1$ and $\mathbf{e}_2$ are unit vectors and Δx is the isotropic grid spacing. A cell is classified as "inside" the material if $\xi(\mathbf{x}) \leq 0$ and "outside" otherwise. This averaging remains numerically stable; by expanding the defined sparse field from G_1 to G_3, we ensure that extreme floating-point values from opposite sides of the interface never appear in the same summation, preventing precision loss or overflow.

For simulated (ϕ^S) and target (ϕ^T) profiles defined on identical grids, a mismatch occurs at cell $\mathbf{x}$ if the inside/outside classifications differ, i.e., when $[\xi^S(\mathbf{x}) \leq 0] \neq [\xi^T(\mathbf{x}) \leq 0]$.[1] The total area difference is computed as:

$$\mathrm{AD}(\phi^S, \phi^T) = \sum_{\mathbf{x} \in G} \left[[\xi^S(\mathbf{x}) \leq 0] \neq [\xi^T(\mathbf{x}) \leq 0] \right] \Delta x^2. \tag{6}$$

The algorithm exhibits $O(N^D)$ time complexity, where D is the spatial dimension and N is the number of grid cells along each dimension.

To address specific device requirements, the implementation supports spatially dependent weighting within the level-set domain. By applying a weight $\rho(\mathbf{x})$ to the cell area, users can emphasize critical regions:

$$\mathrm{AD}_\rho = \sum_{\mathbf{x} \in G} \rho(\mathbf{x}) \left[[\xi^S(\mathbf{x}) \leq 0] \neq [\xi^T(\mathbf{x}) \leq 0] \right] \Delta x^2. \tag{7}$$

This allows for increased sensitivity in functional regions, such as the channel area in transistor profiles or the contact interface in high-aspect-ratio trenches.

[1] $[\cdot]$ is the Iverson bracket defined as $[P] = \begin{cases} 1 & \text{if } P \text{ is true;} \\ 0 & \text{otherwise.} \end{cases}$

3.2 Sparse field distance

The AD measure treats all non-overlapping regions equally, which can be a limitation in complex optimization scenarios. Two simulated profiles with identical total area mismatch may represent distinct levels of convergence. For instance, a profile with a small uniform lateral offset may yield the same AD as a profile that matches the target exactly in some regions, but exhibits large deviations in others (e.g., poor depth reproduction).

This motivates the development of a point-wise SDM that compares signed distance function values directly. By evaluating the continuous field ϕ rather than binary occupancy indicators, a measure can achieve sub-grid accuracy and enhanced sensitivity to local shape variations. The Sparse Field Distance (SFD) leverages the level-set representation to detect subtle geometric differences otherwise overlooked by area-based approaches.

Calculating the SFD requires ensuring that the target profile $\mathcal{T}$ and simulated profile $\mathcal{S}$ share a common computational domain. As discussed in Sect. 2.1, the profiles are represented as sparse fields $\phi^\mathcal{T}$ and $\phi^\mathcal{S}$. Direct point-by-point comparison is only possible where both fields have defined values in the sparse HRLE structure. Thus, one grid must be expanded to ensure coverage: Either $G_1^\mathcal{T} \subset G_{w_\mathcal{S}}^\mathcal{S}$ or $G_1^\mathcal{S} \subset G_{w_\mathcal{T}}^\mathcal{T}$ must hold, where $G_{w_\cdot}$ denotes the expanded region.

This leads to two distinct versions of the SFD:

$$\mathrm{SFD}^\mathcal{S} = \sqrt{\frac{1}{\left|G_1^\mathcal{S}\right|} \sum_{\mathbf{x} \in G_1^\mathcal{S}} \left(\phi^\mathcal{S}(\mathbf{x}) - \phi^\mathcal{T}(\mathbf{x})\right)^2} \tag{8}$$

$$\mathrm{SFD}^\mathcal{T} = \sqrt{\frac{1}{\left|G_1^\mathcal{T}\right|} \sum_{\mathbf{x} \in G_1^\mathcal{T}} \left(\phi^\mathcal{S}(\mathbf{x}) - \phi^\mathcal{T}(\mathbf{x})\right)^2} \tag{9}$$

Both formulations are independent of w, provided the inclusion requirement is satisfied. To assist the user, visualization tools are integrated [23] and a safety mechanism ensures that violations of the inclusion requirement yield a large penalty value to maintain objective function stability.

The choice between these versions involves a trade-off between computational efficiency and optimization robustness. Calculating $\mathrm{SFD}^\mathcal{S}$ involves expanding the target profile $G_1^\mathcal{T}$ only once per optimization run, which is highly efficient. In contrast, computing $\mathrm{SFD}^\mathcal{T}$ requires expanding the simulated profile $G_1^\mathcal{S}$ after every simulation. Since an optimization may involve thousands of iterations, this repeated expansion carries a higher computational cost.

However, $\mathrm{SFD}^\mathcal{S}$ exhibits a significant disadvantage: The number of sampling points $|G_1^\mathcal{S}|$ varies with the simulated geometry. This leads to a critical failure mode when the simulation produces a feature much smaller or shallower than

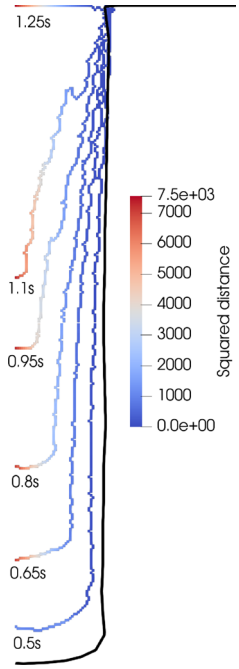

Fig. 3 The experimental target profile (black) and simulated profiles with a given polymer deposition time (color-coded by the squared distance at a given point of the sparse field as calculated in $\mathrm{SFD}^{\mathcal{S}}$). Half of a trench was simulated with a reflective boundary condition on the axis of symmetry

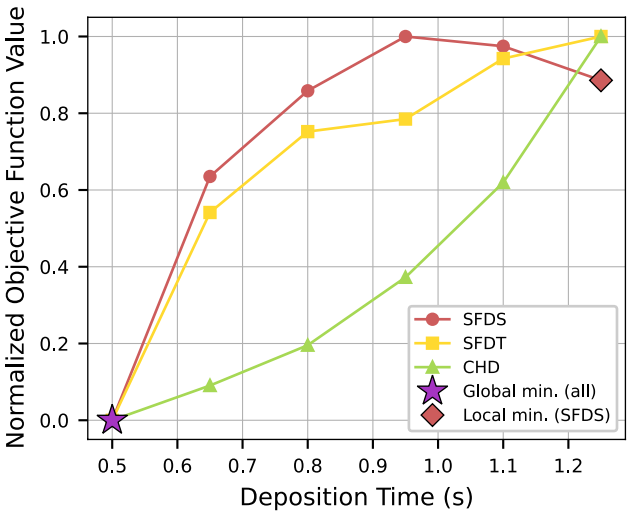

Fig. 4 Demonstration of a local minimum of $\mathrm{SFD}^{\mathcal{S}}$ for the profiles shown in Figure 3

the target, such as a trench that fails to etch deeply due to excessive polymer deposition during DRIE. In these cases, the points at the bottom of the prematurely shallow simulated trench are not compared against the distant target floor; instead, they are matched to the target's upper sidewalls, which happen to be the nearest points on the target surface. This geometric misattribution results in a deceptively low loss value and leads to an undesired local minimum in the objective function. We verified this through a computational experiment on the etching profile shown in Fig. 3, showing the local minimum in Fig. 4. Consequently, $\mathrm{SFD}^{\mathcal{S}}$ is unsuitable for robust calibration; we therefore focus exclusively on $\mathrm{SFD}^{\mathcal{T}}$ (hereafter referred to as SFDT), which ensures the entire target geometry is always accounted for.

3.3 Hausdorff and chamfer distances

The most prominent SDMs in the fields of computer vision and machine learning are the Hausdorff and the Chamfer distances [7, 24, 25]. The Hausdorff distance (HD) for two sets of discrete points A and B is defined as:

$$\mathrm{HD}(A,B) = \max\left(\max_{a\in A} \min_{b\in B} \|a-b\|_2, \max_{b\in B} \min_{a\in A} \|b-a\|_2 \right) \tag{10}$$

While HD identifies the maximum deviation between sets, its non-differentiability and extreme sensitivity to outliers limit its utility as an optimization objective for predictive models. In such applications, the Chamfer distance (CHD) is generally preferred [26]. Unlike HD, the CHD provides a bidirectional measure of shape dissimilarity by quantifying the average nearest-neighbor distances between point sets, making it more robust for gradient-based or stochastic optimization.

Given two point sets representing the surfaces of target and simulated profiles, $\mathcal{P}^{\mathcal{T}} = \{\mathbf{p}_i^{\mathcal{T}}\}_{i=1}^{N_{\mathcal{T}}}$ and $\mathcal{P}^{\mathcal{S}} = \{\mathbf{p}_j^{\mathcal{S}}\}_{j=1}^{N_{\mathcal{S}}}$, extracted from their respective level set representations, the RMS version of the Chamfer distance is defined as:

$$\mathrm{CHD}(\mathcal{P}^{\mathcal{T}},\mathcal{P}^{\mathcal{S}}) = \sqrt{\frac{1}{N_{\mathcal{T}}+N_{\mathcal{S}}}\left(\sum_{i=1}^{N_{\mathcal{T}}} \min_j \|\mathbf{p}_i^{\mathcal{T}}-\mathbf{p}_j^{\mathcal{S}}\|_2^2 + \sum_{j=1}^{N_{\mathcal{S}}} \min_i \|\mathbf{p}_j^{\mathcal{S}}-\mathbf{p}_i^{\mathcal{T}}\|_2^2\right)} \tag{11}$$

Unlike AD and SFDT, the CHD operates on explicit surface points rather than on implicit grid values. This requires a preprocessing step to extract the zero-level set from the sparse field representation. To ensure a valid surface extraction, a minimum bandwidth of two grid cells is required; the framework automatically expands the defined region if this condition is not met. To maintain computational efficiency, the extracted points are organized into k-d tree data structures for fast nearest-neighbor queries. This reduces the computational complexity from $O(N_{\mathcal{T}}N_{\mathcal{S}})$ for a naive brute-force approach to $O(N \log N)$, where $N = N_{\mathcal{T}} + N_{\mathcal{S}}$.

4 Results and validation

To evaluate the performance and robustness of the proposed SDMs, we present two distinct case studies: a cyclic Deep Reactive Ion Etching (DRIE) process and a Plasma-Enhanced Chemical Vapor Deposition (PECVD). While these examples are not an exhaustive catalog of all semiconductor fabrication steps, which would be computationally and length prohibitive, they represent two of the most critical and geometrically challenging scenarios in modern TCAD calibration.

The DRIE case study focuses on the resolution of fine, periodic features (scalloping), where local CD measurements often fail to capture the full profile evolution. The PECVD case study, conversely, demonstrates the measures' ability to seamlessly calibrate to experiments with varying degrees of conformality of the deposited layer. By applying our SDMs to these representative benchmarks, we demonstrate that the transition from discrete sampling to global shape comparison provides a significant increase in calibration accuracy and optimizer stability across diverse fabrication processes.

4.1 DRIE optimization

DRIE is a cyclic process where each iteration isotropically etches a small portion of the substrate, resulting in characteristic sidewall scalloping. Figure 5a shows an experiment involving the first five cycles. Resolving these fine features and their evolution with depth is a significant challenge for traditional CD measurements, making SDMs highly valuable for model calibration.

In this work, the calibration focuses on the chemical and ion-enhanced plasma etching component of the cycle. The underlying etching model is based on the work of Belen et al. [27], which was adapted and implemented within the ViennaPS framework [10, 28, 29]. To maintain computational efficiency during optimization, the polymer deposition and breakthrough phases of the DRIE cycle are treated via emulation, while the physics-based parameters of the SF_6 -driven etch phase are the primary subjects of the calibration.

To evaluate the suitability of these SDMs as objective function, we performed 40 optimization runs with 1000 simulations each. Four objectives were compared: the RMS of the critical dimensions (as defined in Equation 1), AD, CHD, and SFDT. For the CD approach, four points were tracked: trench depth, depth at quarter-width, and widths at the second and fourth scallops. We utilized the `dlib find_min_global` optimizer [30, 31] for ten runs per objective. The decision variables and their respective bounds are detailed in Table 1.

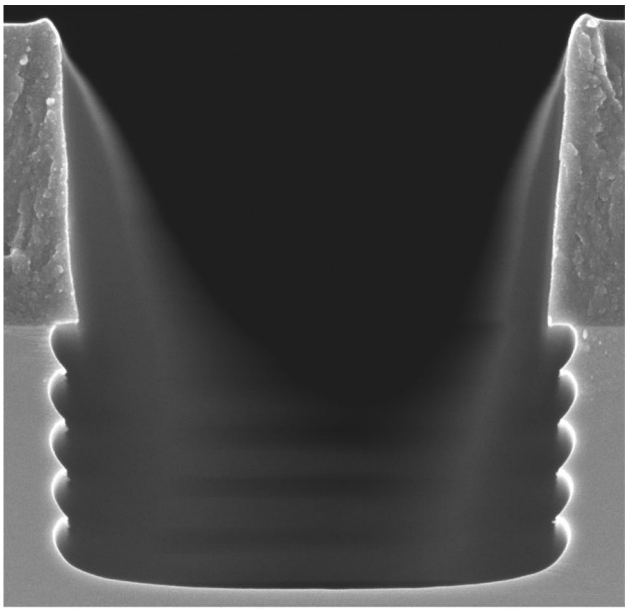

(a) SEM of the first five DRIE cycles (Hard mask on Si).

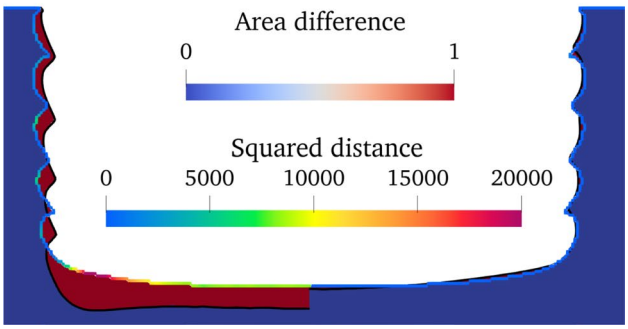

(b) Comparison of a candidate (left) and optimized (right) solution. The black line indicates the simulated surface, while the red-shaded region denotes the AD. The rainbow-colored band represents the sparse field of the experimental surface, color-coded by the squared distance to the simulation using the SFDT method.

Fig. 5 DRIE process optimization results: **a** experimental SEM and **b** comparison with simulated profiles

We analyzed the resulting dataset to determine intra-run trade-offs: when a specific SDM reaches its optimum, how far are the other measures from their respective best values in that same run? The results are summarized in Fig. 6 and Table 2.

As expected, the CD-based approach shows the highest average degradation (46.2%), confirming that optimizing for discrete points often leaves the global profile poorly matched. AD shows moderate trade-offs (19.8%). In striking

Table 1 Optimization decision variables and their respective ranges.

Decision Variable	Unit	Lower Bound	Upper Bound
Breakthrough depth	nm	1.0	150.0
Ion flux	$10\times^{15}$ /cm^2/s	1.0	100.0
F radical flux	$10\times^{15}$ /cm^2/s	5000.0	20000.0
Ion mean energy	eV	10.0	200.0
Ion exponent	—	1.0	1000.0
F radical sticking coefficient	—	0.00001	0.1

Table 2 Intra-run trade-off analysis showing percentage degradation from each measure's best value when the row's measure is optimized.

Optimized	CD	AD	CHD	SFDT	Avg. Others
CD	0.0*	22.5	38.0	78.2	46.2
AD	36.1	0.0*	8.5	14.8	19.8
CHD	25.2	3.9	0.0*	0.5	9.8
SFDT	34.9	3.3	0.1	0.0*	12.8

Table 3 Spearman Correlation Coefficients between Dissimilarity Measures.

Measure	AD	CD	CHD	SFDT
AD	1.00	0.991	0.998	0.998
CD	0.991	1.00	0.988	0.989
CHD	0.998	0.988	1.00	0.999
SFDT	0.998	0.989	0.999	1.00

contrast, CHD and SFDT exhibit minimal trade-offs (9.8% and 12.8%, respectively). This demonstrates that CHD and SFDT are highly representative of the overall geometric state. Optimizing for either measure naturally drives all other evaluated SDMs toward their respective optima. These findings confirm the robustness of CHD and SFDT as primary objective functions for profile matching, effectively overcoming the limitations of the sampling-based methods prevalent in current literature.

The differences are substantial despite high Spearman correlation coefficients between the measures, shown in Table 3. Furthermore, Fig. 7 and Table 4 show that while SFDT is the most computationally expensive SDM, this evaluation time remains a negligible fraction of the total process simulation time.

4.2 SiO^2 PECVD with TEOS

To demonstrate the applicability of our methods to deposition processes, we calibrated a model for the plasma-enhanced chemical vapor deposition (PECVD) of silicon dioxide from tetraethyl orthosilicate (TEOS). This process is fundamental to semiconductor manufacturing, specifically for gap-fill and interlayer dielectric formation [32]. The step coverage and conformality of TEOS deposition create complex profiles that vary significantly with aspect ratio and local transport effects [33]. Traditional CD-based characterization fails to capture these conformality variations, which are critical for device performance and reliability [3, 4].

Figure 8 illustrates the application of the SFDT measure to the TEOS PECVD model implemented in ViennaPS [10]. The annotated (and colored) SEM image highlights the deposited SiO^2 layer (yellow) on a structured substrate (violet). The process parameters, as described in the model documentation [29], were optimized using the `dlib find_min_global` optimizer [30, 31] with a budget of 1,000 evaluations.

The SFDT measure proved particularly effective for this deposition process. Unlike area-based or point-wise measures, the SFDT provides sub-grid sensitivity to local film

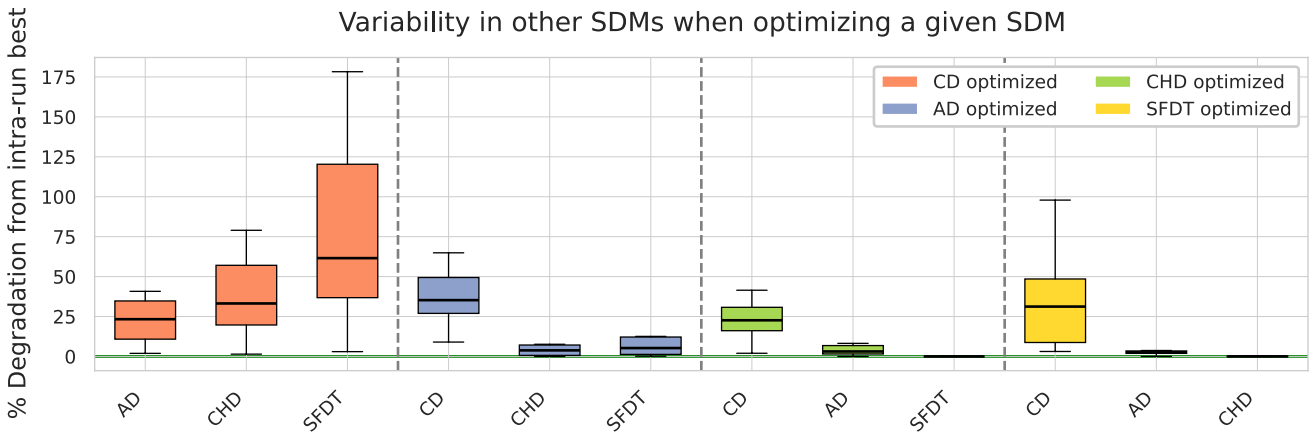

Fig. 6 Intra-run tradeoff analysis of the SDMs

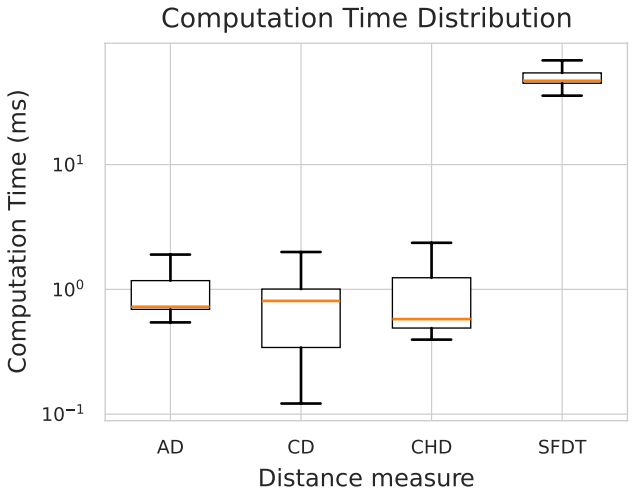

Fig. 7 Distribution of computation time for the evaluated measures

Table 4 Computation time as a percentage of total process execution time.

AD	CD	CHD	SFDT
0.03%	0.02%	0.02%	1.43%

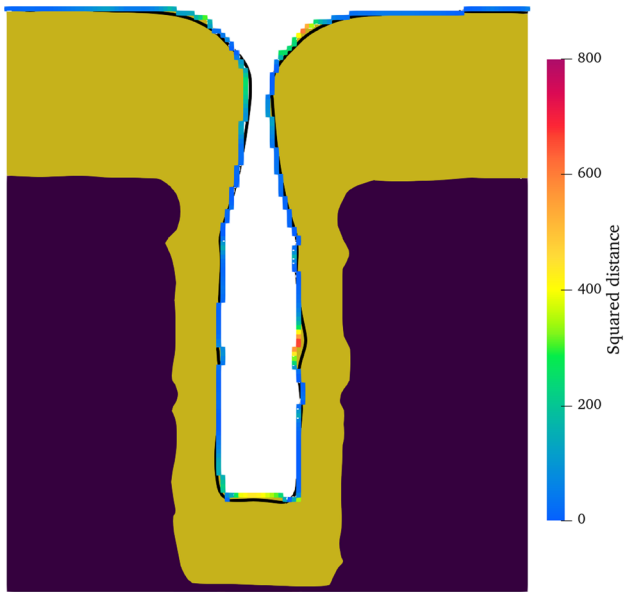

Fig. 8 Optimized PECVD simulation result. The colored SEM highlights the experimental SiO^2 layer (yellow) and substrate (violet). The black line denotes the optimal simulated surface, while the rainbow band represents the SFDT sparse field, indicating the local squared distance between the experimental and simulated profiles

thickness variations across the entire profile. This enabled rapid convergence to physically meaningful parameter sets that accurately reproduce both the overall deposition volume and the fine-scale thickness gradients at the trench corners, regions where device reliability is most often compromised.

5 Discussion

The results from the DRIE and PECVD case studies demonstrate that global SDMs, specifically SFDT and CHD, provide a more stable and physically representative objective function landscape than traditional CD-based methods. The minimal intra-run trade-offs observed for these measures suggest they capture the “true" geometric state of the profile, effectively acting as a proxy for all other geometric metrics. This eliminates the need for the subjective and time-consuming selection of specific critical dimensions, which often vary between different process steps or even different trench geometries.

From an implementation standpoint, the framework is designed to be future-proof. While the current industry standard relies on 2D cross-sections, the underlying C++ implementation utilizes template specialization to support 3D-to-3D geometric comparisons. This ensures that as characterization techniques like FIB-SEM tomography become more common, the transition to full 3D calibration will require no architectural changes to the software. Furthermore, the inclusion of Python bindings for the high-performance geometric kernels in ViennaLS allows them to be integrated into broader automated workflows and modern data science libraries, such as those utilized during optimization runs in ViennaFit.

5.1 Limitations and future work

A primary bottleneck for the widespread adoption of automated calibration remains the scarcity of large-scale, high-quality experimental datasets. While SDMs like SFDT and CHD are designed to fully utilize the geometric information available in a single image, thereby providing a more descriptive objective function than sparse CD sampling, the statistical robustness of a calibrated model is ultimately bounded by the number and diversity of the provided experimental references. In the semiconductor industry, high-resolution TEM and SEM imaging are resource-intensive processes, often resulting in “small data” scenarios that challenge the stability of high-dimensional optimization. Consequently, these robust SDMs are essential not just for accuracy, but for providing the high-sensitivity objective function needed to guide models when only a few “gold standard” images are available.

Furthermore, the transition from raw experimental images to the mathematical boundaries used by our framework represents an important practical consideration. As described in Sect. 2.2, ViennaFit supports both manual boundary annotation and automated extraction via classical edge detection, providing accessible pathways for profile acquisition across a range of image qualities. Nevertheless, these approaches

still require user intervention and domain knowledge, which limits throughput in high-volume scenarios. Future work will focus on deeper integration of automated boundary extraction tools leveraging modern deep-learning architectures for semantic segmentation, to directly provide input for the ViennaLS geometric engines used within the ViennaFit optimization environment. Establishing a fully autonomous "image-to-optimized-model" pipeline will be critical for scaling these methods to support high-volume manufacturing and rapid process screening.

6 Conclusions

We have developed and validated a suite of shape-aware dissimilarity measures that provide a robust, standardized alternative to traditional critical dimension (CD) selection in TCAD model calibration. By shifting the focus from discrete point-wise sampling to global profile matching, we have demonstrated that measures such as the Sparse Field Distance (SFDT) and Chamfer Distance (CHD) yield more consistent optimization trajectories and overcome the geometric ambiguities inherent in local descriptors.

The suite of shape-aware dissimilarity measures, implemented within the ViennaLS library bridges the gap between process simulation and 2D experimental characterization, offering a scalable solution for modern semiconductor manufacturing. As experimental datasets grow in complexity and volume, these SDMs establish the necessary mathematical foundation for automated, machine-learning-driven model training, positioning TCAD for the next generation of data-centric process development.

Author Contributions R.K. led the work, contributing to conceptualization, methodology, software development, theoretical framework, data analysis, validation, writing of the original draft and editing of the manuscript. T.R. contributed to software development and conceptualization. S.D.N. provided experimental data. M.K. contributed to conceptualization and experimental data. P.M. contributed to conceptualization and editing of the manuscript. L.F. acquired funding and contributed to conceptualization, methodology, software and editing of the manuscript. All authors reviewed the manuscript.

Funding Open access funding provided by TU Wien (TUW). Financial support by the Federal Ministry of Labour and Economy, the National Foundation for Research, Technology and Development, and the Christian Doppler Research Association is gratefully acknowledged.

Data Availability The results are fully reproducible with our established open-source tools. Furthermore, the data utilized in these experiments will be made available upon reasonable request.

Declarations

Competing Interests The authors declare no competing interests.

References

1. Krüger, F., Zhang, D., Luan, P., Park, M., Metz, A., Kushner, M.J.: Autonomous hybrid optimization of a SiO_2 plasma etching mechanism. J. Vac. Sci. Technol., A **42**(4), 043008 (2024). https://doi.org/10.1116/6.0003554
2. Huang, S., Panneerchelvam, P., Huard, C.M., Sridhar, S., Ventzek, P.L.G., Smith, M.D.: Process optimization for shallow trench isolation etch using computational models. J. Vac. Sci. Technol., A **41**(5), 053004 (2023). https://doi.org/10.1116/6.0002838
3. Asenov, A., Kaya, S.: Effect of oxide interface roughness on the threshold voltage fluctuations in decanano MOSFETs with ultrathin gate oxides. In: 2000 International Conference on Simulation Semiconductor Processes and Devices (Cat. No.00TH8502), pp. 135–138. IEEE, Seattle, WA, USA (2000). https://doi.org/10.1109/SISPAD.2000.871226
4. Vitiello, J., Piallat, F.: Alternative deposition solution for cost reduction of TSV integration. In: 2018 IEEE 68th Electronic Components and Technology Conference (ECTC), pp. 2163–2167 (2018). https://doi.org/10.1109/ECTC.2018.00324 . ISSN: 2377-5726
5. Nishizuka, T., Igosawa, R., Yokoyama, T., Sako, K., Moki, H., Honda, M.: Precise and practical 3D topography simulation of high aspect ratio contact hole etch by using model optimization algorithm. J. Vac. Sci. Technol., A **42**(4), 043003 (2024). https://doi.org/10.1116/6.0003515
6. Sun, M., Shi, Y., Yang, H., Li, Q., Liu, Q., Zhang, Q., Tang, B., Yang, T., Li, J., Yin, H., Wang, X., Luo, J., Wang, W.: Impact of tin thickness uniformity on the reliability of n-finfets. IEEE Journal of the Electron Devices Society PP, 1–1 (2025) https://doi.org/10.1109/JEDS.2025.3612160
7. Barrow, H.G., Tenenbaum, J.M., Bolles, R.C., Wolf, H.C.: Parametric correspondence and chamfer matching: two new techniques for image matching. In: Proceedings of the 5th International Joint Conference on Artificial Intelligence - Volume 2. IJCAI'77, pp. 659–663. Morgan Kaufmann Publishers Inc., San Francisco, CA, USA (1977). https://www.ijcai.org/Proceedings/77-2/Papers/024.pdf Accessed 2026-02-04
8. Klemenschits, X., Reiter, T., Karnel, N., Filipovic, L.: ViennaLS: High-performance sparse level-set library for topography simulations. GitHub repository (2026). https://github.com/ViennaTools/ViennaLS
9. Reiter, T., Filipovic, L.: ViennaPS: A flexible framework for semiconductor process simulation. SoftwareX 32, 102453 (2025) https://doi.org/10.1016/j.softx.2025.102453
10. Reiter, T., Kostal, R., Karnel, N., Filipovic, L.e.a.: ViennaPS. GitHub repository (2026). https://github.com/ViennaTools/ViennaPS
11. Adalsteinsson, D., Sethian, J.A.: A level set approach to a unified model for etching, deposition, and lithography I: Algorithms and

two-dimensional simulations. J. Comput. Phys. **120**(1), 128–144 (1995). https://doi.org/10.1006/jcph.1995.1153
12. Radjenović, B., Lee, J.K., Radmilović-Radjenović, M.: Sparse field level set method for non-convex Hamiltonians in 3D plasma etching profile simulations. Comput. Phys. Commun. **174**(2), 127–132 (2006). https://doi.org/10.1016/j.cpc.2005.09.010
13. Osher, S., Sethian, J.A.: Fronts propagating with curvature-dependent speed: Algorithms based on Hamilton-Jacobi formulations. J. Comput. Phys. **79**(1), 12–49 (1988). https://doi.org/10.1016/0021-9991(88)90002-2
14. Whitaker, R.T.: A Level-Set Approach to 3D Reconstruction from Range Data. Int. J. Comput. Vision **29**(3), 203–231 (1998). https://doi.org/10.1023/A:1008036829907
15. Houston, B., Nielsen, M.B., Batty, C., Nilsson, O., Museth, K.: Hierarchical RLE level set: A compact and versatile deformable surface representation. ACM Trans. Graph. **25**(1), 151–175 (2006). https://doi.org/10.1145/1122501.1122508
16. Ertl, O.: Numerical methods for topography simulation, Technische Universität Wien (2010). https://doi.org/10.34726/hss.2010.001 . (Thesis)
17. Kostal, R., Filipovic, L.: ViennaFit: A Python package for fitting ViennaPS models to experimental data. GitHub repository (2026). https://github.com/ViennaTools/ViennaFit
18. Canny, J.: A computational approach to edge detection. IEEE Trans. Patt. Anal. Mach. Intell. PAMI **8**(6), 679–698 (1986). https://doi.org/10.1109/tpami.1986.4767851
19. Bradski, G.: The OpenCV library. Dr. Dobb's Journal 25(11), 120–125 (2000). Num Pages: 5. Accessed 2026-04-28
20. Wang, F., Yu, H., Miao, Y., Sun, K., Sun, Y., Yang, H., Li, X.: AI-driven feature recognition of SEM profiles in deep reactive ion etching based on physics-constrained variational autoencoder. Microsyst. Nanoeng. **12**(1), 82 (2026). https://doi.org/10.1038/s41378-025-01105-z
21. Bunday, B., Bishop, M.R., Mccormack, D., Villarrubia, J.S., Vladar, A., Vorburger, T.V., Orji, N.G., Allgair, J.: Determination of Optimal Parameters for CD-SEM Measurement of Line Edge Roughness. NIST **5375**, 515–533 (2004)
22. Lorusso, G.F., Rutigliani, V., Van Roey, F., Mack, C.A.: Unbiased roughness measurements: Subtracting out SEM effects. Microelectron. Eng. **190**, 33–37 (2018). https://doi.org/10.1016/j.mee.2018.01.010
23. Kitware, I.: ParaView. https://www.paraview.org/. Version 6.0.1 (2025)
24. Hausdorff, F.: Grundzüge der Mengenlehre. Veit & Comp., Leipzig (1914). English translation: *Set Theory*, Chelsea Publishing, 1957
25. Huttenlocher, D.P., Klanderman, G.A., Rucklidge, W.J.: Comparing images using the Hausdorff distance. IEEE Trans. Pattern Anal. Mach. Intell. **15**(9), 850–863 (1993). https://doi.org/10.1109/34.232073
26. Fan, H., Su, H., Guibas, L.: A Point Set Generation Network for 3D Object Reconstruction from a Single Image. In: 2017 IEEE Conference on Computer Vision and Pattern Recognition (CVPR), pp. 2463–2471 (2017). https://doi.org/10.1109/CVPR.2017.264 . ISSN: 1063-6919
27. Belen, R.J., Gomez, S., Cooperberg, D., Kiehlbauch, M., Aydil, E.S.: Feature-scale model of Si etching in SF6/O2 plasma and comparison with experiments. J. Vac. Sci. Technol., A **23**(5), 1430–1439 (2005). https://doi.org/10.1116/1.2013317
28. Bobinac, J., Reiter, T., Piso, J., Klemenschits, X., Baumgartner, O., Stanojevic, Z., Strof, G., Karner, M., Filipovic, L.: Effect of mask geometry variation on plasma etching profiles. Micromachines **14**(3), 665 (2023). https://doi.org/10.3390/mi14030665. Publisher: Multidisciplinary Digital Publishing Institute
29. Reiter, T., al.: ViennaPS Documentation. https://viennatools.github.io/ViennaPS/models/ (2026)
30. King, D.E.: Dlib-ml: A machine learning toolkit. J. Mach. Learn. Res. 10, 1755–1758 (2009). Accessed 2026-02-04
31. King, D.E.: dlib C++ Library: `find_min_global` Documentation. https://dlib.net/dlib/global_optimization/find_max_global_abstract.h.html#find_min_global. Accessed: 2026-05-01 (2017)
32. Ray, S.K., Maiti, C.K., Lahiri, S.K., Chakrabarti, N.B.: TEOS-based PECVD of silicon dioxide for VLSI applications. Adv. Mater. Opt. Electron. **6**(2), 73–82 (1996). https://doi.org/10.1002/(SICI)1099-0712(199603)6:2<73::AID-AMO215>3.0.CO;2-R
33. Su, M., Yu, D., Liu, Y., Wan, L., Song, C., Dai, F., Xue, K., Jing, X., Guidotti, D.: Properties and electric characterizations of tetraethyl orthosilicate-based plasma enhanced chemical vapor deposition oxide film deposited at 400°C for through silicon via application. Thin Solid Films **550**, 259–263 (2014). https://doi.org/10.1016/j.tsf.2013.11.002